C: Physical Processes in Nanomaterials and Nanostructures

Redox Modifications of Carbon Dots Shape Their Optoelectronics

Ranjan Kumar Behera, Abhishek Sau, Leepsa Mishra, Kallol Bera, Samapika Mallik, Alpana Nayak, Samita Basu, and Manas Kumar Sarangi

J. Phys. Chem. C, **Just Accepted Manuscript** • DOI: 10.1021/acs.jpcc.9b08289 • Publication Date (Web): 17 Oct 2019

Redox Modifications of Carbon Dots Shape their Optoelectronics

Ranjan Kumar Behera[#], Abhishek Sau[†$], Leepsa Mishra[#], Kallol Bera[†&], Samapika Mallik[#], Alpana Nayak[#], Samita Basu[†], Manas Kumar Sarangi*[, #]

[#]Department of Physics, Indian Institute of Technology Patna, India

[†]Chemical Sciences Division, Saha Institute of Nuclear Physics Kolkata, India

Corresponding Author

* mksarangi@iitp.ac.in

Present Addresses:

[$]Department of Molecular and Cellular Medicine, Texas A&M University, USA,

[&]Division of Biology & Biological Engg, California Institute of Technology, Pasadena, USA

Abstract:

Carbon dots (CDs) are 1-10 nm scaled complex nanostructures with a wide range of applications and show unconventional photophysical behavior upon excitation. In this article, we have unveiled some of the underlying mechanisms and excited state dynamics of CDs by perturbing their interface with oxidizing and reducing agents. With no substantial alteration in size of surface treated oxidized (^{O}CDs), reduced (^{R}CDs) and untreated CDs (^{U}CDs), we observe marked changes in their charge transport properties and diverse spectral signatures in singlet and triplet excited states. Fine tuning of the spectral behavior of nanomaterials is often treated as an outcome of quantum confinement of the excitons. Herein with different spectroscopic techniques along with conducting atomic force microscopy and triplet-triplet absorption, we elucidate that, not just confinement, the structural modification at the surface also dictates optoelectronic behavior by altering some properties like energy bandgap, quantum tunneling across metal-CD-metal junction and yield of triplet excitons.

Introduction:

For more than a decade since their discovery by Scrivens et al., fluorescent carbon nanodots (CDs) have become one of the most promising fluorophores of the carbon family[1]. The unique properties of CDs like water solubility, stability, tunable photo-physics, low toxicity, easy and inexpensive preparation, have garnered much attention among the scientific and industrial communities for potential applications such as sensing[2-4], imaging[5-8], catalysis[9], medicine[10-11], optoelectronics[12-15], energy conversion and storage[16-18]. Although a variety of "top-down" and "bottom-up" approaches has been developed to synthesize the CDs, the origin of their luminescent behavior is still an open question[19-20]. Several recent reports suggest that the photo-luminescent (PL) behavior can be tuned by altering the synthetic technique, temperature, size, starting precursor, doping, surface functionalization etc.[21-26] For example, while many CDs show excitation wavelength dependent PL (EDPL), a direct violation of the Kasha-Vavilov's rule[27-28], there also exist reports of excitation independent PL behavior (EIPL) in CDs.

CDs have many advantages over the conventional semiconductor quantum dots[13]. However, a large-scale application of CDs in biotechnology and optoelectronics demands a critical and clear understanding of the electronic structure, various radiative and non-radiative pathways upon their photo-excitation[12-14]. Based on different experimental and theoretical studies on CDs, several hypotheses have been proposed to explain the intricacy and origin of their photo-physical nature. Size dependent optical properties of graphitic CDs is often ascribed to the quantum confinement of the photo-generated exciton in the π-conjugated carbon core[21-26]. With the increase in the size of the CDs, the π-conjugation becomes even more predominant with a decrease in the bandgap. This results in tunable PL, with red-shifting of the emission maxima, as particle size increases[23-24]. The narrowing of the bandgap with an increase in the size of CDs strongly affects the quantum yield and average lifetime of the exciton. Formation of more defect sites in larger CDs facilitates the non-radiative electron trapping at the defect sites leading to a significant drop in PL intensity of CDs. Another well accepted hypothesis for the PL of CDs is ascribed to the surface mediated changes regulating its optical property. While the core of the CDs consists of sp^2 hybridization, the surface is often surrounded by carbon with dangling functional groups like C-O, C=O, C-O-C, O=C-O-H, etc. [29]. It is believed that these functional groups act like surface energy traps and restricts the radiative decay pathway by trapping the generated photo-excited electrons. Removing the surface energy traps by surface passivation of the dangling ends often leads to an enhancement of PL by increasing the radiative decay from the surface traps, and hence increasing the excited state lifetime and quantum yield[28, 30]. Several modifications to the CDs surface have been reported in the literature to tune the PL intensity[19-20]. The excitation dependent PL of some CDs are due to the presence of multiple emissive states. Surface passivation with varied functional groups modulates the EDPL of CDs, for example, CDs surfaces with amine rich functional groups show

EIPL property, while CDs with lower or no amine functional groups on the surface show a strong dependence on the excitation wavelength[31-32].

Photo-bleaching, toxicity, high costs and inefficient charge separations of holes and electrons in some organic dyes often limit their applications for photovoltaics, LEDs and other optoelectronic devices. CDs doped solar cells, CDs-ZnO nano-particle composites, N-doped and P-doped CDs have been reported to enhance the photoelectric conversion efficiency in many fabricated devices[17, 33-36]. Several studies of CDs for electroluminescence and LEDs have also been reported due to their high photostability and quantum yield as well as inherent flexibility in designing different variants[36-38]. However, detailed excited state behavior and the varied conducting properties of CDs at the nanoscale are still lacking. For instance, the interplay of the various modes of radiative and non-radiative relaxation pathways for CDs is complex and depends on their core structure, size, surface modifications, etc. Similarly, the exciton/charge carrier formation upon photoexcitation, carrier mobility, parent spin state (singlet or triplet) of formation and electron-hole recombination as well as their luminescence efficiency remain elusive. While the properties of the electronically injected charge carriers in the singlet excited states have been studied with some clarity, the studies on excited triplet states and the probable recombination rates of triplet and singlet excitons are very limited[28, 30]. A better understanding of the plausible singlet and triplet states along with their photo-dynamics, bandgap and intersystem crossing (ISC) can open up more choices for modification and design for higher luminescence efficiency and hence their uses in LEDs and optoelectronics[39-42]. In this article, with a variety of steady-state and time-resolved spectroscopic techniques and conductivity measurements, we have attempted to unveil the interplay of these excited state behavior and the tuning of the electronic band structure of native and redox modified CDs. We believe these intriguing upshots will address some of the very fundamental yet unanswered questions and may open up new avenues for their optoelectronic applications.

Experimental section: All the solvents and chemicals required for the synthesis of carbon dots (CDs) are of analytical grade. The citric acid (CA) (≥99.5%, anhydrous), sodium borohydride ($NaBH_4$) (≥99.5%) and hydrogen peroxide (H_2O_2) are purchased from Merck and used without further purification. For the preparation of all the aqueous solutions, we have used Milli-Q (MQ) water. Solvents required for synthesis and spectroscopic studies have been purchased from Sigma Aldrich.

***(a)* Synthesis of ^{U}CDs:** ^{U}CDs are hydrothermally synthesized by pyrolyzing 1.0 gm of CA dissolved in 10 ml of MQ water at 140 ^{o}C for 5 hours. After 5 hours, the solution is converted to brownish-yellow gel-like material. Then, the product is lyophilized and run through a silica gel column with 1:1 EtOH: DCM mixture, and dried by rotary-evaporator resulting in a yellow-colored product. The product is further purified by HPLC size exclusion column chromatography (Superdex-75, EtOH is used as elution solvent) followed by lyophilization and has been used for further experiments. The elution fraction from the most intense peak of the elution profile is collected (Figure-S1) and used for the rest of the spectroscopic and microscopic experiments. (a) *Synthesis of ^{R}CDs:* 20 mg of synthesized ^{U}CDs are taken in 10 ml of MQ water. Aqueous sodium borohydride (0.038 gm, 100 mM) solution is added and kept overnight to confirm the completion

of the reaction. Then, the solution is lyophilized and purified by silica gel chromatography (1:1 EtOH: DCM mixture) followed by HPLC as above. (b) *Synthesis of ^{O}CDs:* 20 mg of synthesized ^{U}CDs are taken in 10 ml of MQ water. 3 ml of 30 % of hydrogen peroxide (in excess) is added, the reaction mixture is closed with a lid and kept at room temperature till the completion of the reaction. Then, the solution is lyophilized and purified by silica gel chromatography followed by HPLC as explained earlier.

(b) Steady-state measurements: Steady-state absorption spectra and photoluminescence spectra are recorded by JASCO V-650 absorption spectrophotometer and Spex-fluoromax-3 spectro-fluorimeter, respectively. Quartz cuvettes with 10 mm path length are used for both UV-vis and PL measurements. The fluorescence quantum yield (ϕ) is measured keeping quinine sulfate in 0.1M H_2SO_4 (Quantum yield, 0.54) by using the following formula (equation-1). Fourier transform infrared (FTIR) spectra of the CDs are recorded using a PerkinElmer spectrum 400 spectrometer in ATR mode. All steady-state measurements are performed at room temperature with baseline and inner filter corrections.

$$\phi_F = \phi_R \times \frac{I_F}{I_R} \times \frac{O.D_R}{O.D_F} \times \left\{\frac{\eta_F}{\eta_R}\right\}^2 \text{.....(1)}$$

Where ϕ is the quantum yield; *I* is the integrated fluorescence intensity; O.D is the optical density, and η is the refractive index. The subscript R and F represent the reference and fluorophore quinine sulfate and CDs respectively.

(c) Time-Correlated Single-Photon Counting (TCSPC): Time-resolved emission spectra are detected by using a picosecond pulsed diode laser-based TCSPC spectrometer and MCP-PMT as a detector[43-45]. The emission from the sample is collected at a right angle to the direction of the excitation beam, maintaining the magic angle polarization with a bandpass of 4 nm. Full-width half maximum of the instrument response function is 270 ps, with a channel resolution of 28ps/channel. The data are fitted to the multi-exponential function after de-convoluting the IRF signal using IBH DAS 6.2 data analyzer software, in which reduced χ^2 and weighted residuals serve as the parameter for the goodness of the fit. The standard deviations are calculated to be below 10% of the measured value.

(d) Laser Flash Photolysis: The transient intermediates are generated with third harmonics output of nanosecond flash photolysis setup (applied Photo-physics) containing Nd: YAG (Lab series, model lab 150, spectra Physics) in which the sample is excited at 355 nm (FWHM = 8 ns) laser light[46-48]. A pulsed xenon lamp (150 W) is used to monitor the transient species in the triplet through the absorption of light. The photomultiplier (1P28) output is supplied into a Tektronix oscilloscope (TDS 3054B, 500 MHz, 5 Gs/sec) and the data are transferred to a computer using TEKVISA software. The samples are de-gassed by-passing pure argon gas for 20 mins before each experiment. All the steady-state and time-resolved measurements are performed at room temperature (298 K). The ORIGIN 8.5 software is used for plotting the data as well as for fitting the decay curves.

(e) Transmission Electron Micrograph (TEM): Transmission electron microscopic measurements are performed using aFEI, Tecnai G2 F30, S-Twin microscope operating at 300 kV equipped with a GATAN Orius SC1000B CCD camera. For clean monolayer sample preparation, we have used a simple technique on a 300-mesh carbon-coated copper grid and followed a drop-casting method. For drying purposes, we have kept the grid for 24 hours in a vacuum condition. After complete drying, the grid is used for TEM measurements and processed through ImageJ software.

(f) Atomic Force Microscope (AFM): Topography images are taken in the non-contact mode of AFM (model: Agilent Technologies 5500). Silicon cantilevers with resonance frequency 289 kHz and spring-constant 42 N/m are used. Current-sensing atomic force microscope (CS-AFM) measurements are done in contact mode using a gold-coated cantilever (spring constant~0.2 N/m and tip radius ~10 nm) in ambient condition. The load force is maintained below 10 nN to avoid damage to the cantilever tip. For I-V measurements, the bias voltage is applied to the sample (ITO glass plate) while the tip is grounded. The bias voltage is swept from -10.0 V to +10.0 V with a sweep rate of 200 mV/s. Before performing I-V, the surface is scanned to locate a particle, and then the tip is placed over a single particle to carry out I-V measurement. The instrument has a limit to measure the current up to 10nA. We have used WSxM 5.0 developer 8.3 software to process the AFM images and ORIGIN 8.5 version software to plot the CS-AFM data.

(g) Film preparation for AFM: Synthesized ^{U}CDs, ^{R}CDs, and ^{O}CDs solutions are deposited on silicon wafer by spin-coating method. Silicon(100) wafers are cleaned by ultra-sonication in acetone for 5 mins, followed by 5 mins of sonication in MQ water. The substrate is dried at room temperature and spin-coated with the CDs solutions at 500 rpm for 60 sec. All procedures for film preparation are conducted at room temperature (25° C) and normal relative humidity. The spin-coated CDs on silicon wafers are analyzed with AFM in non-contact mode using SSS-NCH silicon tips. For I-V characterization, CDs solutions are deposited on ITO coated glass plate. For CS-AFM, the same spin coating process is used to deposit CDs on the ITO coated glass plate, with PPP-NCH Au coated cantilever for scanning the image as well as for I-V measurements of various CDs.

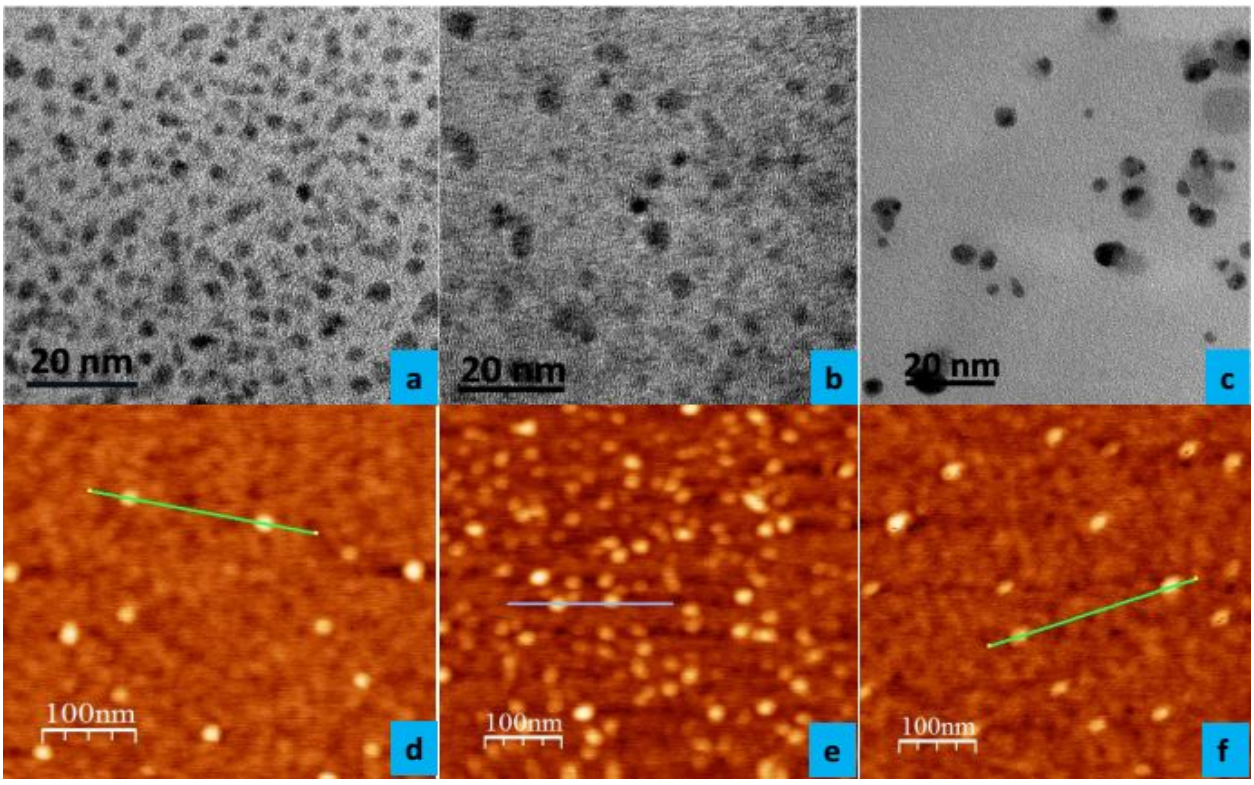

Figure 1: High-resolution transmission electron micrographs (HR-TEM) (a, b, c) and Atomic force microscopy images (d, e, f) of ^{U}CDs, ^{O}CDs and ^{R}CDs are shown in the top and bottom panel respectively. Details of the size distribution and height profiles are in Figure-S2.

Results and Discussion: Figure-1 provides the relative sizes of the ^{U}CDs, ^{O}CDs and ^{R}CDs measured from HR-TEM (Figure-1a, 1b and 1c) and AFM (Figure-1d, 1e and 1f) respectively. Their size distributions and features (Figure-S2) reflect an average dimension of ~ 4 nm for the HR-TEM and ~ 6 nm for AFM image along with a 2 nm height profile. This indicates that the overall size of CDs does not show any significant change with surface modifications. However, their spectroscopic features (Figure-2) show distinct changes in molecular structure, ground state and excited state behavior. A comparison of the FTIR spectra shows characteristic changes in the native and the surface modified CDs with the appearance of new peaks corresponding to new stretching frequencies as shown in Figure-2a. FTIR spectra of ^{O}CDs (red) exhibit a new peak w.r.t ^{R}CDs, and ^{U}CDs located at 2840 cm^{-1} that is allied with the =C−H stretching frequency of aldehyde (-CH=O) functional group indicates H_2O_2 mediated oxidation of primary alcohol (-CH_2OH). FTIR spectra of ^{R}CDs exhibit two new peaks at 952 and 1184 cm^{-1} w.r.t. ^{O}CDs and ^{U}CDs are associated with newly formed alkene =C−H bending vibration and alcohol C-O stretching frequency, indicating a partial reduction of the accessible poorly reactive alkyne (2113 cm^{-1}) and reactive carbonyl (1638 cm^{-1}) towards $NaBH_4$.

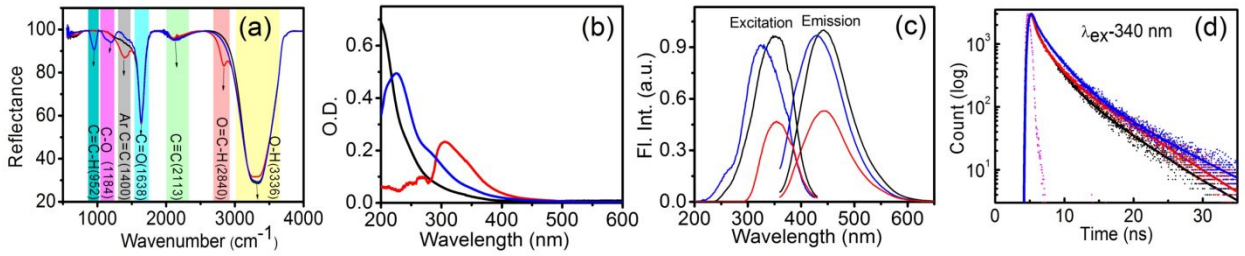

Figure 2: (a) FTIR spectra, (b) absorption spectra, (c) fluorescence emission spectra at (λ_{ex} =340 nm) along with excitation spectra at their corresponding emission maxima, and (d) lifetime decays of ^{U}CDs (black), ^{O}CDs (red) and ^{R}CDs (blue) (at λ_{ex} =340 nm) at their respectively emission maxima.

Steady-state absorption and fluorescence for various types of CDs have been conducted in an aqueous medium. ^{U}CDs show a wide range of absorption from 200 to 400 nm similar to the reported values in the literature[21]. This is often ascribed to the typical absorption from HOMO to LUMO of an aromatic π-system or the π- π* transition (high energy blue end) and n- π* transition (low energy red end) of carbonyl group present within the CDs. ^{R}CDs show similar absorption as ^{U}CDs with a small red-shift in their absorption maxima. On the contrary, ^{O}CDs have a significant reduction in the π→π* transition with negligible absorption up to 280 nm, however, the n→π* transition shows an increment around 310 nm (Figure-2b). The characteristic changes in the UV-vis spectra show that the π-conjugated system in CDs and their transitional features are heavily perturbed with surface modification by $NaBH_4$ and H_2O_2. The emission spectra of ^{U}CDs, ^{R}CDs and ^{O}CDs at 340nm excitation along with the corresponding excitation spectra at their respective emission maxima are shown in the Figure-2c. The emission spectra of the CDs are mostly symmetrical on the wavelength scale, mirroring their excitation spectra with a large Stokes shift of ~ 90 nm. While the excitations for ^{U}CDs and ^{R}CDs for their respective emission maxima have a very wide range of excitation from 200-400 nm, the ^{O}CDs have excitation only after 300nm for their emissive maxima. Taking quinine sulfate as a standard, the quantum yields of ^{U}CDs, ^{R}CDs and ^{O}CDs are observed to be 0.08, 0.11 and 0.02 respectively[27]. This hints at a feature of less emissive states in the blue region for ^{O}CDs, compared to ^{U}CDs and ^{R}CDs, and also counts for the relatively less quantum yield of ^{O}CDs compared to others. Though not very straight forward, a common assumption of origin of PL of CDs is from the excitation of the sp^2-core (core emission) and the sp^3 carbon matrix (surface emission) with dangling functional groups like C-O, C=O, C-O-C, O=C-O-H etc[49]. The surface dangling bonds trap the excitons and increase the non-radiative pathways. $NaBH_4$ treatment reduces the carbonyl to the hydroxyl group and decreases the number of trapped sites. H_2O_2 treatment, on the other hand, enhances the number of trapped sites, resulting in a drop in quantum yield. This is well supported by our lifetime measurements where for excitation at 375 nm, the average lifetime for ^{U}CDs is 4.2 ns (Figure-2d, S3, S4 and Table-S1). Treating CDs with $NaBH_4$ enhances the lifetime to 4.9 ns and the treatment with H_2O_2 reduces it 4.0 ns. Moreover, all the fluorescence decay profiles fit to three-exponentials, with long component (τ^1) of ~7 ns, medium (τ^2) 2-3 ns and fast component (τ^3) of the order of few hundred ps (Figure-S3, S4 and Table-S1). The amplitudes and contributions of the three components for ^{U}CDs, ^{R}CDs and ^{O}CDs vary with the excitation wavelength and depend upon the nature of the emissive species.

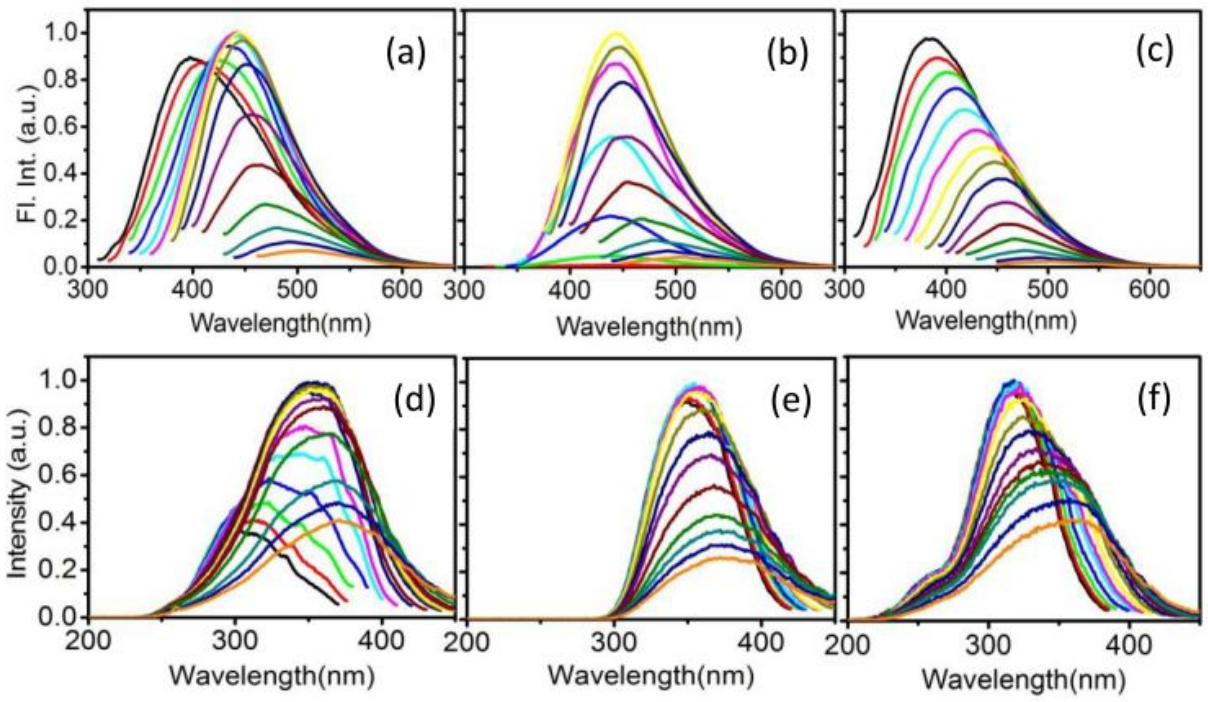

Figure 3: Panel (a, b, c): Normalised steady-state fluorescence spectra of ^{U}CDs, ^{O}CDs and ^{R}CDs with increasing excitation wavelength from 280 nm to 420 nm with an increment of 10 nm (color from 280-420 nm are black, red, green, blue, cyan, magenta, yellow, dark yellow, navy, purple, wine, olive, dark cyan, royal, orange respectively). Panel (d, e, f): Excitation spectra of ^{U}CDs, ^{O}CDs and ^{R}CDs for their respective emission maxima (from the top panel). The color codes of excitation spectra correspond with their emission spectra.

Steady-state emission peaks for the ^{U}CDs and ^{R}CDs are found to be dependent upon the excitation wavelength, while the behavior for ^{O}CDs is found to be more or less independent of excitation wavelength (Figure-3). Excitation dependent PL (EDPL) is not uncommon for CDs, though its origin is still debatable, we hypothesize that the EDPL for ^{U}CDs and ^{R}CDs are cumulating emission from multiple excited species and different surface emissive states. With the gradual increase in the excitation wavelength from the blue end to red, the PL profiles for CDs show red-shifting with maximum intensity for λ_{ex}= 350 nm, and a steady decrease in PL intensity afterward (Figure-3a). Contrary to ^{U}CDs and ^{R}CDs, we observe mostly an EIPL behavior for ^{O}CDs with a gradual increase in intensity followed by a drop, with an increase in λ_{ex} (Figure-3b). As we go to the red region of the excitation, we observe the appearance of the EDPL. For ^{R}CDs, we observe a steady decline in the intensity with redshift, as the excitation wavelength is varied from the blue to red end (Figure-3c). To better understand the diverse EDPL behavior of the CDs, and to quantify the contribution from the excited species, we have measured the excitation spectra for ^{U}CDs (Figure-3d), ^{O}CDs (Figure-3e) and ^{R}CDs (Figure-3f) at their respective emission maxima. Figure-3d reflects that the excitation maxima for ^{U}CDs consist over a wide range from 270-380 nm, showing that cumulative absorption for the entire envelope comprises of wide possibility n-π* and π-π* transitions in the nanocore and dangling surface. The reduction of ^{U}CDs shows a shift in the excitation maxima from 320-360 nm (Figure-3f). This indicates that $NaBH_4$ treatment on the surface has eliminated many

high energy transitions compared to ^{U}CDs. On the other hand for ^{O}CDs, the broad distribution of excitation maxima has been narrowed to a single peak around 360 nm like a single fluorophore, with excitation starting only after 300nm as shown in Figure-3e. This eliminates most of the high energy π-π* transitions and allowing only the n-π* transitions, which explains the EIPL behavior of ^{O}CDs, as most of the transitions for ^{O}CDs are n-π* in nature, with almost no contribution from π-π* transitions. Both the steady-state and time-resolved spectroscopic characterizations clearly state that, even though the sizes of ^{U}CDs, ^{R}CDs and ^{O}CDs remain similar, the PL properties display diverse properties upon redox alteration and are originating from multiple chromophore units[40].

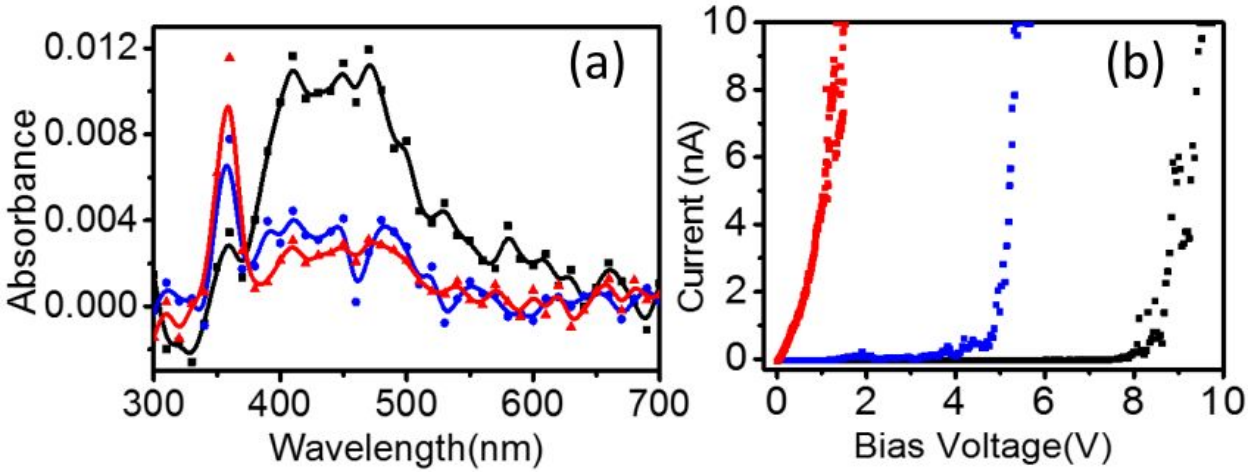

Figure 4: (a) Transient triplet-triplet (T-T) absorption spectra of (λ_{ex} = 355 nm) ^{U}CDs, ^{O}CDs and ^{R}CDs (black, red, blue) respectively. (b) Electrical properties: Current (nA) vs. Voltage (V) curve for forward regions of ^{U}CDs (black), ^{O}CDs (red), ^{R}CDs (blue) and their fittings respectively from CS-AFM (Insert)

A thorough understanding of the excitonic properties, not just in the singlet (S) states but also in the triplet (T) state is needed for a complete picture of the dynamics of the photo-excited CDs. The absolute populations of the two spin states, the S and T states are the measures of the rates of ISC quantum yield, energy bandgap between the two spin states and spin-orbit coupling[27], which ultimately fine-tune the electronic and optical quantum efficiency. Uoyama et al. successfully enhanced the electroluminescence efficiency of organic-based LEDs (OLEDs) by altering spin conversion efficiency with a series of desired modifications on several donor-acceptor molecules[41-42]. By cleverly designing the band gap between the S and T excited states, they were able to harness the intrinsic fluorescence efficiency over 90%. The efficiencies of third generations OLEDs have been improved to unity by regulating the recombination of the S and T state excitons, with thermally activated delayed fluorescence[50-51]. Herein, to understand spin states populations and electronic transition behavior of ^{U}CDs, ^{R}CDs and ^{O}CDs, we have attempted to probe and characterize the triplet states populations by ns-time-resolved T-T absorption spectroscopy (Figure-4a) and the electrical conductivity by CS- AFM measurements (Figure-4b) respectively. A typical transient T-T absorption spectrum shows two absorption maxima, one at 360 nm (peak-I) and a relatively broad peak around 400-500 nm (peak-II). Although the amplitude of peak-II is predominantly high for ^{U}CDs, the peak is substantially reduced for the surface treated ^{R}CDs and ^{O}CDs with the emergence of peak-I along with a distinct iso-absorption point at 370 nm. The

presence of two T-T absorption peaks for the ^{U}CDs indicates that, triggering the laser flash and consequent probing by pulsed xenon open up two possible transitions in the triplet state to the higher excited states. The variations in the amplitudes for the peaks for the ^{R}CDs and ^{O}CDs compared to ^{U}CDs are a consequence of the differential transition rates of the two possible states from T^1 to a higher energy triplet states T^n on surface modifications. To explain the subtleties of the transitions in the three CDs, we propose a model based on the selection rules to access for all the possible allowed triplet states (Scheme-1). CDs are composed of several >C=C< and >C=O bonds, therefore normal ($\pi \rightarrow \pi^*$, $n \rightarrow \pi^*$) transitions are quite favorable in the ground state. Figure-2b shows a very wide range of (S^0-S^1) absorption comprising of several $\pi \rightarrow \pi^*$ and $n \rightarrow \pi^*$ transitions under UV-visible illumination. The ISC from the excited S to probable T is often governed by spin selection rules, energy bandgap and the exchange interaction energy between S-T states. Moreover, certain direct transitions like S^1 (n, π^*) to T^1 (n, π^*) and S^1 (π, π^*) to T^1 (π, π^*) are restricted by El-Sayed rule[52-53]. Keeping all these in mind, our proposed scheme traces out the possible triplet (n, π^*) and (π, π^*) states from both S^1 (n, π^*) and S^1 (π, π^*). This resembles our experimental observation of two distinct absorption bands in T-T spectra. The broad range of peak-II suggests a wide variation in triplet absorption (n, π^*), as absorption by multiple chromophoric units in the singlet states (π-π^*) cannot be ruled out. This behavior of CDs has been extensively reported in the literature and is often considered to be the origin of EDPL for CDs. The non-bonding electrons on –OH and >C=O as well as the π electrons in the aromatic moieties are likely to be affected by the surface modification using H_2O_2 and $NaBH_4$. This leads to a drop in the singlet π-π^*, hence, after ISC we observe reduced intensity in triplet n- π^* (peak-II) for ^{R}CDs and ^{O}CDs. In the absence of the redox reagents, the π - π^* in the singlet is sufficiently high to generate enough triplet n-π^* (peak-I) through ISC for ^{U}CDs. The increased absorption for ^{U}CDs in peak-II is supported by a higher lifetime of 2.53 µs at 470 nm compared to 1.84 µs for ^{O}CDs and 1.88 µs for ^{R}CDs (Figure-5, S5, Table-S2). A concomitant decrease in the lifetime of 1.81 µs for ^{U}CDs at 360 nm (peak-I, triplet π-π^*) is observed, while the lifetimes for ^{O}CDs and ^{R}CDs are enhanced to 2.25 and 2.18 µs respectively. This is a clear indication of alteration of the dynamics of the multiple excited transition states for the >C=C< and >C=O bonds, and the isosbestic point at 375 nm establishes the equilibrium between the two forms in the triplet states, due to keto-enol tautomerism in the CDs upon surface modification [45, 49, 54-56].

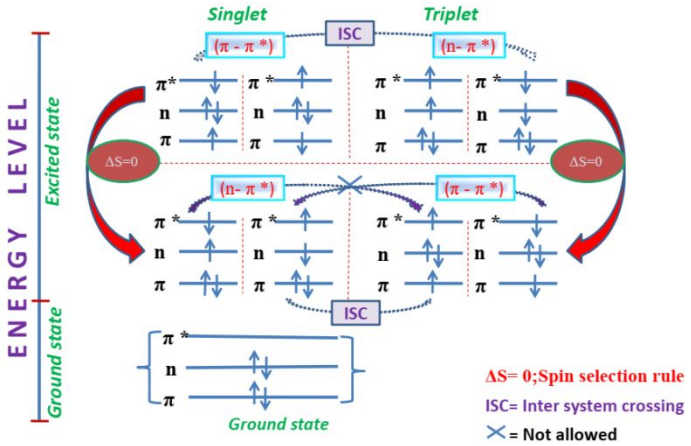

Scheme-1: The proposed mechanism between singlet and triplet inter system crossing based on possible allowed transitions.

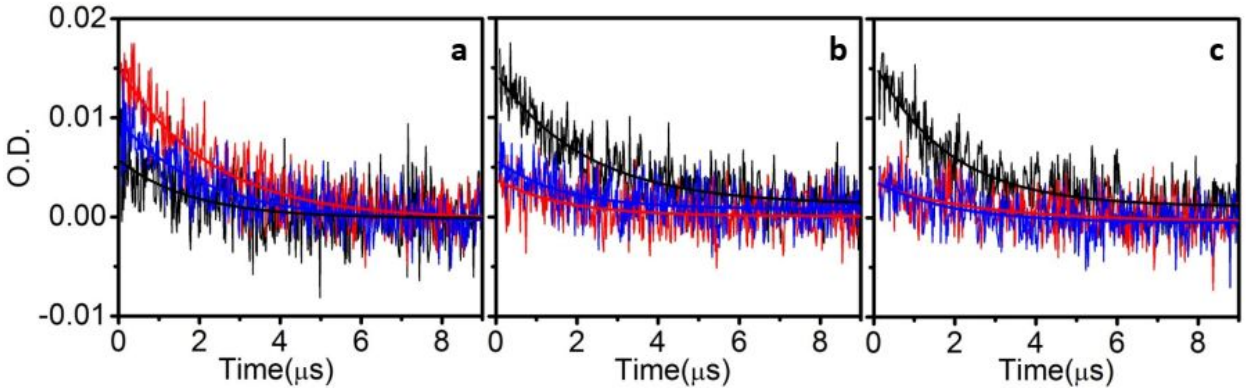

Figure 5: The triplet decay fits for ^{U}CDs (black), ^{O}CDs (red), and ^{R}CDs (blue) at (a) 360 nm (b) 410 nm and (c) 470 nm respectively.

To understand the impact of surface perturbations before and after treatment with $NaBH_4$ and H_2O_2 on the charge transport properties, well dispersed CDs on a surface are studied by CS-AFM[57-58]. CS-AFM is capable of providing direct information on topography, surface conductivity, dopant profiling, barrier height and local electronic states of the quantum-confined nanoscale materials[59-61]. The conducting tip of AFM makes electrical contact with the surface of CDs, which leads to the formation of a metal-CD-metal junction. The tunneling current at the contact point is often regarded as a direct measure of the height and width of the energy barrier across the junction. Typical I-V characteristics obtained with identical measurement conditions by placing the AFM tip on ^{U}CD, ^{R}CD, and ^{O}CD, respectively, deposited on ITO-coated glass are shown in Figure-4b, S6 and Table-S3. As can be seen, for a given forward bias, the level of current is much higher for the ^{O}CDs than those for the ^{R}CDs and ^{U}CDs. While the ^{U}CDs show negligible current (~pA) until about 8V, the ^{R}CDs show significant current at about 4 V. In contrast to ^{U}CDs and ^{R}CDs; the ^{O}CDs show rapid increase in current even for bias as small as 50 mV. All of these I-Vs follow exponential functions. The value of constant A from the FN equation is used to calculate the barrier height (φ_b) by the following relation.

$$I(v) = Bv^2\, e^{-A/v} \text{.....(2)}$$

$$\text{Where } B = \frac{A_{eff} e^3 m^*}{8\pi h \varphi_b d^2 m} \text{ and } A = \frac{8\pi d\sqrt{2m^*}\,\varphi_b^{3/2}}{3he} = 6.83 d \sqrt{\frac{m^*}{m}}\varphi_b^{3/2}$$

φ_b = contact barrier height, d = separation between two electrodes or thickness of the particle, A_{eff} = effective contact area, m^* = effective mass of electron, m = mass of electron, h = Planck's constant, v = applied voltage, I =current through the junction.

The value of constant A for ^{U}CDs, ^{R}CDs, and ^{O}CDs are 18.32 ±0.6, 15.34 ±0.7, 4.70 ±0.01 respectively. For the sake of simple calculation, we have assumed $\frac{m^*}{m}$ as unity and the thickness

(d) for CDs are 2nm. The dI/dV curves (shown in supporting information, Figure-S7) indicates conduction gaps of 10 eV and 5 eV for the metal-^{U}CD-metal and metal-^{R}CD-metal junctions, respectively. However, the ^{O}CDs showed markedly different behavior with a negligible conduction gap. These observations indicate that the redox treatments modify the density of states at the Fermi level to such an extent that the conductivity of ^{O}CDs and ^{R}CDs become substantially higher than the ^{U}CDs due to the inclusion of additional charge carriers after surface modification. Although the trend of conduction gaps is consistent with that of band gaps obtained from UV-vis spectroscopy (4.22, 3.41, and 3.1 eV for ^{U}CDs, ^{R}CDs and ^{O}CDs, respectively, Figure-S8), the subtle difference in their values can be attributed to the fact that the spectroscopy method gives an average property of CDs in solution, whereas CS-AFM gives local information of a single CD structure on a surface. Further analyses of I-Vs are carried out to investigate the charge transport mechanisms and the energy barriers in these CD systems. From topography images, it is clear that there is no significant change in the sizes of CDs upon surface modifications. This suggests that the barrier width for charge transport, which depends on the size, does not vary. However, the barrier height, which depends on the surface modifications causing changes in the density of states, varies significantly. To estimate the barrier height across the metal-CD-metal junction, the I-V curves are analyzed with the Fowler-Nordheim (F-N) tunneling model given by equation-2[62]. The details of the fitting parameters are provided in Figure-S6 and Table-S3. The fittings indicate tunneling to be the possible mechanism for charge transport. Further, from the F-N plots, the values of φ_b for the ^{U}CDs, ^{R}CDs and ^{O}CDs are estimated to be 1.21, 1.07 and 0.5 eV, respectively. These values are in good agreement with the trend of band gaps obtained from UV-vis spectroscopy, which also follow a decreasing order for ^{U}CDs, ^{R}CDs and ^{O}CDs respectively. It is interesting to note that the barrier height for ^{R}CDs is about 11.6 % smaller, but for ^{O}CDs, it is about 58.7 % smaller than that of ^{U}CDs. This remarkable decrease in barrier height of ^{O}CDs indicates the profound effects of surface modifications and demands further investigation to justify the role of the redox processes involved.

In different nanomaterials, variations in the shapes and sizes of the nano-structures are responsible for the changes in the barrier height, often attributed to the quantum confinement effect, which severely alters their optical and electrical properties. Herein for nano-confined CDs, we observe a new approach to alter the bandgap based on surface modifications. While the sizes of the ^{U}CDs, ^{R}CDs and ^{O}CDs show no reasonable variations, with surface modifications, we have modulated the bandgaps of the ^{U}CDs, ^{R}CDs and ^{O}CDs. We propose that for CDs, not just quantum confinement of the excitons, but surface modifications and relative changes in the different emissive states of the nanodots determine the tune-ability of their optical and also electrical properties.

Conclusions

Potential large scale uses of CDs in the field of optoelectronics necessitate a complete understanding of the interplay of photo-induced S and T state excitons and charge transfer in the tailored zero-dimensional nanodots. By concomitant changes in the trapped surface states with redox reagents, we have modulated the spectral behavior without any marked alteration to their physical dimensions. From the T-T absorption, we have precisely predicted the underlying

intersystem crossing mechanism for the transiently populated S and T excitonic species for the surface modified CDs upon laser excitation. The local electrical conductivity measurements of the ^{U}CDs, ^{R}CDs and ^{O}CDs using CS-AFM provide a better understanding of the charge transport properties at the nanoscale across the metal-CD-metal junction. We find that the I-V curves fit well with the Fowler-Nordheim tunneling model indicating the electron tunneling to be a possible mechanism for charge transport. Moreover, ^{O}CDs show remarkably small barrier height for tunneling as compared to the ^{R}CDs system. This emphasizes the impact of redox based surface modifications on the electronic structure of the CDs systems.

Associated Contents:

The Supporting Information is available free of charge on the ACS Publications website: Details of the distributions of the particles, PL lifetimes and their distributions, Triplet lifetimes, fitting parameters of I-V curves and its derivatives are shown in the supporting information.

Acknowledgments

The authors acknowledge the Science and Engineering Research Board, Govt. of India, for Research grant under sanction ECR/2016/002036. RKB and LM acknowledge fellowships from IIT Patna and SERB respectively. We greatly acknowledge the generous support from TEM division of Saha Institute of Nuclear Physics for providing the research facility for TEM measurements.

Conflict of Interest: The authors declare no conflict of interest.

References

1. Xu, X.; Ray, R.; Gu, Y.; Ploehn, H. J.; Gearheart, L.; Raker, K.; Scrivens, W. A., Electrophoretic Analysis and Purification of Fluorescent Single-Walled Carbon Nanotube Fragments. *Journal of the American Chemical Society* **2004,** *126* (40), 12736-12737.
2. Sun, H.; Wu, L.; Wei, W.; Qu, X., Recent Advances in Graphene Guantum Dots for Sensing. *Mater. Today* **2013,** *16* (11), 433--442.
3. Sun, X.; Lei, Y., Fluorescent Carbon Dots and their Sensing Applications. *TrAC, Trends Anal. Chem.* **2017,** *89*, 163--180.
4. Pan, L.; Sun, S.; Zhang, A.; Jiang, K.; Zhang, L.; Dong, C.; Huang, Q.; Wu, A.; Lin, H., Truly Fluorescent Excitation-Dependent Carbon Dots and Their Applications in Multicolor Cellular Imaging and Multidimensional Sensing. *Adv. Mater.* **2015,** *27* (47), 7782--7787.
5. Cao, L.; Wang, X.; Meziani, M. J.; Lu, F.; Wang, H.; Luo, P. G.; Lin, Y.; Harruff, B. A.; Veca, L. M.; Murray, D. *et. al.*, Carbon Dots for Multiphoton Bioimaging. *Journal of the American Chemical Society* **2007,** *129* (37), 11318-11319.
6. Yang, S.-T.; Cao, L.; Luo, P. G.; Lu, F.; Wang, X.; Wang, H.; Meziani, M. J.; Liu, Y.; Qi, G.; Sun, Y.-P., Carbon Dots for Optical Imaging in Vivo. *Journal of the American Chemical Society* **2009,** *131* (32), 11308-11309.
7. Zhi, B.; Cui, Y.; Wang, S.; Frank, B. P.; Williams, D. N.; Brown, R. P.; Melby, E. S.; Hamers, R. J.; Rosenzweig, Z.; Fairbrother, D. H.; Orr, G.; Haynes, C. L., Malic Acid Carbon Dots: From Super-resolution Live-Cell Imaging to Highly Efficient Separation. *ACS Nano* **2018,** *12* (6), 5741--5752.
8. Jiang, K.; Sun, S.; Zhang, L.; Lu, Y.; Wu, A.; Cai, C.; Lin, H., Red, Green, and Blue Luminescence by Carbon Dots: Full-Color Emission Tuning and Multicolor Cellular Imaging. *Angew. Chem. Int. Ed.* **2015,** *54* (18), 5360--5363.
9. Liu, X.; Dai, L., Carbon-based Metal-free Catalysts. *Nature Reviews Materials* **2016,** *1*, 16064.
10. Wu, C.; Chiu, D. T., Highly Fluorescent Semiconducting Polymer Dots for Biology and Medicine. *Angew. Chem. Int. Ed.* **2013,** *52* (11), 3086--3109.
11. Li, J.; Yang, S.; Deng, Y.; Chai, P.; Yang, Y.; He, X.; Xie, X.; Kang, Z.; Ding, G.; Zhou, H.*et. al*., Emancipating Target-Functionalized Carbon Dots from Autophagy Vesicles for a Novel Visualized Tumor Therapy. *Adv. Funct. Mater.* **2018,** *28* (30), 1800881.
12. Ren, X.; Liang, W.; Wang, P.; Bunker, C. E.; Coleman, M.; Teisl, L. R.; Cao, L.; Sun, Y.-P., A New Approach in Functionalization of Carbon Nanoparticles for Optoelectronically Relevant Carbon Dots and Beyond. *Carbon* **2019,** *141*, 553--560.
13. Li, X.; Rui, M.; Song, J.; Shen, Z.; Zeng, H., Carbon and Graphene Quantum Dots for Optoelectronic and Energy Devices: A Review. *Adv. Funct. Mater.* **2015,** *25* (31), 4929--4947.
14. Choi, H.; Ko, S.-J.; Choi, Y.; Joo, P.; Kim, T.; Lee, B. R.; Jung, J.-W.; Choi, H. J.; Cha, M.; Jeong, J.-R.*et. al.*, Versatile Surface Plasmon Resonance of Carbon-dot-supported Silver Nanoparticles in Polymer Optoelectronic Devices. *Nat. Photonics* **2013,** *7* (9), 732.
15. Hu, C.; Li, M.; Qiu, J.; Sun, Y.-P., Design and Fabrication of Carbon Dots for Energy Conversion and Storage. *Chem. Soc. Rev.* **2019,** *48* (8), 2315--2337.
16. Briscoe, J.; Marinovic, A.; Sevilla, M.; Dunn, S.; Titirici, M., Biomass-Derived Carbon Quantum Dot Sensitizers for Solid-State Nanostructured Solar Cells. *Angew. Chem. Int. Ed.* **2015,** *54* (15), 4463--4468.
17. Zhang, Y.-Q.; Ma, D.-K.; Zhang, Y.-G.; Chen, W.; Huang, S.-M., N-doped Carbon Quantum Dots for TiO2-based Photocatalysts and Dye-sensitized Solar Cells. *Nano Energy* **2013,** *2* (5), 545--552.
18. Wang, H.; Sun, P.; Cong, S.; Wu, J.; Gao, L.; Wang, Y.; Dai, X.; Yi, Q.; Zou, G., Nitrogen-Doped Carbon Dots for "green" Quantum Dot Solar Cells. *Nanoscale Res. Lett.* **2016,** *11* (1), 27.
19. Lim, S. Y.; Shen, W.; Gao, Z., Carbon Quantum Dots and their Applications. *Chem. Soc. Rev.* **2014,** *44* (1), 362--381.
20. Wang, Y.; Hu, A., Carbon Quantum Dots: Synthesis, Properties and Applications. *J. Mater. Chem. C* **2014,** *2* (34), 6921--6939.
21. Zhu, S.; Song, Y.; Zhao, X.; Shao, J.; Zhang, J.; Yang, B., The Photoluminescence Mechanism in Carbon Dots (graphene quantum dots, carbon nanodots, and polymer dots): Current State and Future Perspective. *Nano Res.* **2015,** *8* (2), 355--381.
22. Yan, Y.; Gong, J.; Chen, J.; Zeng, Z.; Huang, W.; Pu, K.; Liu, J.; Chen, P., Recent Advances on Graphene Quantum Dots: From Chemistry and Physics to Applications. *Adv. Mater.* **2019,** *0* (0), 1808283.
23. Sun, Y.-P.; Zhou, B.; Lin, Y.; Wang, W.; Fernando, K. A. S.; Pathak, P.; Meziani, M. J.; Harruff, B. A.; Wang, X.; Wang, H.*et. al.*, Quantum-Sized Carbon Dots for Bright and Colorful Photoluminescence. *J. Am. Chem. Soc.* **2006,** *128* (24), 7756--7757.
24. Yeh, T.-F.; Huang, W.-L.; Chung, C.-J.; Chiang, I.-T.; Chen, L.-C.; Chang, H.-Y.; Su, W.-C.; Cheng, C.; Chen, S.-J.; Teng, H., Elucidating Quantum Confinement in Graphene Oxide Dots Based On Excitation-Wavelength-Independent Photoluminescence. *J. Phys. Chem. Lett.* **2016,** *7* (11), 2087--2092.
25. Sk, M. A.; Ananthanarayanan, A.; Huang, L.; Lim, K. H.; Chen, P., Revealing the Tunable Photoluminescence Properties of Graphene Quantum Dots. *J. Mater. Chem. C* **2014,** *2* (34), 6954--6960.
26. Hola, K.; Bourlinos, A. B.; Kozak, O.; Berka, K.; Siskova, K. M.; Havrdova, M.; Tucek, J.; Safarova, K.; Otyepka, M.; Giannelis, E. P.*et. al*.., Photoluminescence Effects of Graphitic Core Size and Surface Functional Groups in Carbon Dots: COO− Induced Red-shift Emission. *Carbon* **2014,** *70*, 279--286.
27. *Principles of Fluorescence Spectroscopy | Joseph R. Lakowicz | Springer*.

28. Sau, A.; Bera, K.; Pal, U.; Maity, A.; Mondal, P.; Basak, S.; Mukherjee, A.; Satpati, B.; Sen, P.; Basu, S., Design and Synthesis of Fluorescent Carbon-Dot Polymer and Deciphering Its Electronic Structure. *J. Phys. Chem. C* **2018,** *122* (41), 23799--23807.
29. Fu, M.; Ehrat, F.; Wang, Y.; Milowska, K. Z.; Reckmeier, C.; Rogach, A. L.; Stolarczyk, J. K.; Urban, A. S.; Feldmann, J., Carbon Dots: A Unique Fluorescent Cocktail of Polycyclic Aromatic Hydrocarbons. *Nano Lett.* **2015,** *15* (9), 6030--6035.
30. Sau, A.; Bera, K.; Mondal, P.; Satpati, B.; Basu, S., Distance-Dependent Electron Transfer in Chemically Engineered Carbon Dots. *J. Phys. Chem. C* **2016,** *120* (47), 26630--26636.
31. Yang, C.; Zhu, S.; Li, Z.; Li, Z.; Chen, C.; Sun, L.; Tang, W.; Liu, R.; Sun, Y.; Yu, M., Nitrogen-doped Carbon Dots with Excitation-independent Long-wavelength Emission Produced by a Room-temperature Reaction. *Chem. Commun.* **2016,** *52* (80), 11912--11914.
32. Wang, H.; Sun, C.; Chen, X.; Zhang, Y.; Colvin, V. L.; Rice, Q.; Seo, J.; Feng, S.; Wang, S.; Yu, W. W., Excitation Wavelength Independent Visible Color Emission of Carbon Dots. *Nanoscale* **2017,** *9* (5), 1909--1915.
33. Liu, K.-K.; Li, X.-M.; Cheng, S.-B.; Zhou, R.; Liang, Y.-C.; Dong, L.; Shan, C.-X.; Zeng, H.-B.; Shen, D.-Z., Carbon-ZnO Alternating Quantum Dot Chains: Electrostatic Adsorption Assembly and White Light-emitting Device Application. *Nanoscale* **2018,** *10* (15), 7155--7162.
34. Lee, J. M.; Kwon, B.-H.; Park, H. I.; Kim, H.; Kim, M. G.; Park, J. S.; Kim, E. S.; Yoo, S.; Jeon, D. Y.; Kim, S. O., Exciton Dissociation and Charge-Transport Enhancement in Organic Solar Cells with Quantum-Dot/N-doped CNT Hybrid Nanomaterials. *Adv. Mater.* **2013,** *25* (14), 2011--2017.
35. Jiao, S.; Du, J.; Du, Z.; Long, D.; Jiang, W.; Pan, Z.; Li, Y.; Zhong, X., Nitrogen-Doped Mesoporous Carbons as Counter Electrodes in Quantum Dot Sensitized Solar Cells with a Conversion Efficiency Exceeding 12%. *J. Phys. Chem. Lett.* **2017,** *8* (3), 559--564.
36. Mo, X.; Lu, Q.; Li, T.; Tao, X.; Qi, C.; Zhou, Y.; Jiang, Q.; Ouyang, Y., Low-voltage Multicolor Electroluminescence from All-inorganic Carbon dots/Si-heterostructured Light-emitting Diodes. *J. Mater. Sci.* **2019,** *54* (11), 8492--8503.
37. Zhang, X.; Zhang, Y.; Wang, Y.; Kalytchuk, S.; Kershaw, S. V.; Wang, Y.; Wang, P.; Zhang, T.; Zhao, Y.; Zhang, H. *et. al.* Color-Switchable Electroluminescence of Carbon Dot Light-Emitting Diodes. *ACS Nano* **2013,** *7* (12), 11234--11241.
38. Yuan, F.; Wang, Z.; Li, X.; Li, Y.; Tan, Z. a.; Fan, L.; Yang, S., Bright Multicolor Bandgap Fluorescent Carbon Quantum Dots for Electroluminescent Light-Emitting Diodes. *Adv. Mater.* **2017,** *29* (3), 1604436.
39. Shoaee, S.; Stolterfoht, M.; Neher, D., The Role of Mobility on Charge Generation, Recombination, and Extraction in Polymer-Based Solar Cells. *Adv. Energy Mater.* **2018,** *8* (28), 1703355.
40. Rao, A.; Chow, P. C. Y.; Gélinas, S.; Schlenker, C. W.; Li, C.-Z.; Yip, H.-L.; Jen, A. K.-Y.; Ginger, D. S.; Friend, R. H., The Role of Spin in the Kinetic Control of Recombination in Organic Photovoltaics. *Nature* **2013,** *500* (7463), 435.
41. Goushi, K.; Yoshida, K.; Sato, K.; Adachi, C., Organic Light-emitting Diodes Employing Efficient Reverse Intersystem Crossing for Triplet-to-singlet State Conversion. *Nat. Photonics* **2012,** *6* (4), 253.
42. Uoyama, H.; Goushi, K.; Shizu, K.; Nomura, H.; Adachi, C., Highly Efficient Organic Light-emitting Diodes from Delayed Fluorescence. *Nature* **2012,** *492* (7428), 234.
43. Sarangi, M. K.; Basu, S., Photophysical Behavior of Acridine with Amines within the Micellar Microenvironment of SDS: a Time-resolved Fluorescence and Laser Flash Photolysis Study. *PCCP* **2011,** *13* (37), 16821--16830.
44. Sarangi, M. K.; Mitra, A. K.; Sengupta, C.; Ghosh, S.; Chakraborty, S.; Saha, C.; Basu, S., Hydrogen Bond Sensitive Probe 5-Methoxy-1-keto-1,2,3,4-tetrahydro Carbazole in the Microheterogeneity of Binary Mixtures and Reverse Micelles. *J. Phys. Chem. C* **2013,** *117* (5), 2166--2174.
45. Sarangi, M. K.; Mitra, A.; Basu, S., Prototropic Interactions of Pyrimidine Nucleic Acid Bases with Acridine: A Spectroscopic Investigation. *J. Phys. Chem. B* **2012,** *116* (34), 10275--10282.
46. Sarangi, M. K.; Bhattacharyya, D.; Basu, S., Influence of 2′-Deoxy Sugar Moiety on Excited-State Protonation Equilibrium of Adenine and Adenosine with Acridine inside SDS Micelles: A Time-Resolved Study with Quantum Chemical Calculations. *ChemPhysChem* **2012,** *13* (2), 525--534.
47. Sarangi, M. K.; Dey, D.; Basu, S., Influence of Heterogeneity of Confined Water on Photophysical Behavior of Acridine with Amines: A Time-Resolved Fluorescence and Laser Flash Photolysis Study. *J. Phys. Chem. A* **2011,** *115* (2), 128--135.
48. Sarangi, M. K.; Basu, S., Associated Electron and Proton transfer between Acridine and Triethylamine in AOT reverse Micelles Probed by Laser Flash Photolysis with Magnetic Field. *Chem. Phys. Lett.* **2011,** *506* (4), 205--210.
49. Bera, K.; Sau, A.; Mondal, P.; Mukherjee, R.; Mookherjee, D.; Metya, A.; Kundu, A. K.; Mandal, D.; Satpati, B.; Chakrabarti, O.*et. al.*, Metamorphosis of Ruthenium-Doped Carbon Dots: In Search of the Origin of Photoluminescence and Beyond. *Chem. Mater.* **2016,** *28* (20), 7404--7413.
50. Chen, X.-K.; Kim, D.; Brédas, J.-L., Thermally Activated Delayed Fluorescence (TADF) Path toward Efficient Electroluminescence in Purely Organic Materials: Molecular Level Insight. *Acc. Chem. Res.* **2018,** *51* (9), 2215--2224.
51. Wilson, J. S.; Dhoot, A. S.; Seeley, A. J. A. B.; Khan, M. S.; Köhler, A.; Friend, R. H., Spin-dependent Exciton Formation in π-conjugated Compounds. *Nature* **2001,** *413* (6858), 828--831.
52. Lower, S. K.; El-Sayed, M. A., The Triplet State and Molecular Electronic Processes in Organic Molecules. *Chem. Rev.* **1966,** *66* (2), 199--241.
53. El-Sayed, M. A., Triplet state. Its Radiative and Nonradiative Properties. *Acc. Chem. Res.* **1968,** *1* (1), 8--16.
54. Sun, X.; Li, Y., Colloidal Carbon Spheres and Their Core/Shell Structures with Noble-Metal Nanoparticles. *Angew. Chem. Int. Ed.* **2004,** *43* (5), 597--601.

55. Sevilla, M.; Fuertes, A. B., Chemical and Structural Properties of Carbonaceous Products Obtained by Hydrothermal Carbonization of Saccharides. *Chemistry – A European Journal* **2009,** *15* (16), 4195--4203.
56. Kouras-Hadef, S.; de Sainte-Claire, P.; ter Halle, A.; Amine-Khodja, A.; Richard, C., The Role of Triplet State Keto–Enol Tautomerism in the Photodeamination of Metamitron. *J. Phys. Chem. A* **2011,** *115* (50), 14397--14406.
57. Lang, K. M.; Hite, D. A.; Simmonds, R. W.; McDermott, R.; Pappas, D. P.; Martinis, J. M., Conducting Atomic Force Microscopy for Nanoscale Tunnel Barrier Characterization. *Rev. Sci. Instrum.* **2004,** *75* (8), 2726--2731.
58. Lanza, M., *Conductive Atomic Force Microscopy: Applications in Nanomaterials*. Wiley: 2017.
59. Kelley, T. W.; Granstrom, E.; Frisbie, C. D., Conducting Probe Atomic Force Microscopy: A Characterization Tool for Molecular Electronics. *Adv. Mater.* **1999,** *11* (3), 261--264.
60. Cui, X. D.; Primak, A.; Zarate, X.; Tomfohr, J.; Sankey, O. F.; Moore, A. L.; Moore, T. A.; Gust, D.; Harris, G.; Lindsay, S. M., Reproducible Measurement of Single-Molecule Conductivity. *Science* **2001,** *294* (5542), 571--574.
61. Beebe, J. M.; Kim, B.; Gadzuk, J. W.; Daniel Frisbie, C.; Kushmerick, J. G., Transition from Direct Tunneling to Field Emission in Metal-Molecule-Metal Junctions. *Phys. Rev. Lett.* **2006,** *97* (2), 026801.
62. Nayak, A.; Suresh, K. A., Conductivity of Langmuir-Blodgett films of a Disk-shaped liquid-crystalline molecule–DNA Complex Studied by Current-sensing Atomic Force Microscopy. *Phys. Rev. E* **2008,** *78* (2), 021606.

Table of Contents Graphics: